

EARLY ONLINE RELEASE

This is a PDF of a manuscript that has been peer-reviewed and accepted for publication. As the article has not yet been formatted, copy edited or proofread, the final published version may be different from the early online release.

This pre-publication manuscript may be downloaded, distributed and used under the provisions of the Creative Commons Attribution 4.0 International (CC BY 4.0) license. It may be cited using the DOI below.

The DOI for this manuscript is

DOI:10.2151/jmsj.2019-053

J-STAGE Advance published date: June 28th, 2019

The final manuscript after publication will replace the preliminary version at the above DOI once it is available.

1

2 Revisiting the impact of Stochastic Multicloud Model on the MJO
3 using low-resolution ECHAM6.3 atmosphere model

4 Libin Ma^{1,2}, Karsten Peters^{4,#}, Bin Wang^{2,3,*}, and Juan Li^{1,2}

5

6 1. Key Laboratory of Meteorological Disaster of Ministry of Education (KLME)/Joint
7 International Research Laboratory of Climate and Environment Change
8 (ILCEC)/Collaborative Innovation Center on Forecast and Evaluation of Meteorological
9 Disasters (CIC-FEMD), College of College of Atmospheric Science, Nanjing University
10 of Information Science and Technology, Nanjing 210044, China

11 2. Earth System Modeling Center, College of Atmospheric Science, Nanjing University
12 of Information Science and Technology, Nanjing 210044, China

13 3. Department of Atmosphere and International Pacific Research Center, School of Ocean
14 and Earth Science and Technology, University of Hawaii at Manoa, Honolulu, Hawaii
15 96822, USA

16 4. Max Planck Institut für Meteorologie, #Deutsches Klimarechenzentrum GmbH
17 (DKRZ), Hamburg, Germany

18

19 *Corresponding author: Bin Wang, wangbin@hawaii.edu

20

21

10-08-2018

22

Submitted to JMSJ

23

24

Abstract

25 Based on the preceding work, the influence of the Stochastic Multicloud Model
26 (SMCM) on the Madden-Julian Oscillation (MJO) in the state-of-the-art ECHAM6.3
27 atmosphere general circulation model (AGCM) is further evaluated. The evaluation
28 presented here is based on six recently proposed dynamics-oriented diagnostic metrics.
29 Lag-longitude correlation maps of surface precipitation in the East Indian and West
30 Pacific Oceans confirm the previously found improved representation of the MJO in the
31 modified ECHAM6.3 model compared to the standard configuration. In fact, the
32 modified ECHAM6.3 outperforms the default ECHAM6.3 in five of the six MJO-related
33 diagnostics evaluated here. In detail, the modified ECHAM6.3 (1) successfully models
34 the eastward propagation of boundary layer moisture convergence (BLMC); (2) captures
35 the rearward tilted structure of equivalent potential temperature (EPT) in the lower
36 troposphere and forward tilted structure of EPT in the upper troposphere; (3) exhibits the
37 rearward tilted structure of equatorial diabatic heating in the lower troposphere; (4)
38 adequately simulates the MJO-related horizontal circulation at 850 and 200 hPa as well
39 as the 300 hPa diabatic heating structure. These evaluations confirm the crucial role of
40 convective-parameterization formulation on GCM-simulated MJO dynamics and support
41 the further application and exploration of the SMCM-concept in full-complexity GCMs.

42

43 **Key words:** Madden-Julian Oscillation, ECHAM6.3 atmospheric model, Stochastic
44 Multicloud Model, eastward propagation of Madden-Julian Oscillation, dynamics-
45 oriented diagnosis

46

47 **1. Introduction**

48 The Madden-Julian Oscillation (MJO) is the most pronounced tropical intraseasonal
49 mode of variability (Madden and Julian, 1971, 1972; Zhang, 2005; Waliser et al., 2012).
50 It is characterized by a convective-anomaly envelope propagating eastward with periods
51 of 30-80 days. It mostly originates in the Indian Ocean, propagates eastward and
52 transverses the Maritime Continent and equatorial Pacific Ocean with about 5 m/s
53 (Zhang, 2013; Yoneyama et al., 2013; DeMott et al., 2015).

54 Over the past four decades, the dynamical and thermodynamical structures of the MJO
55 have been well documented by observations and theoretic models (e.g., Madden and
56 Julian, 1971; Madden and Julian, 1972; Rui and Wang, 1990; Weickmann et al., 1985;
57 Wheeler and Kiladis, 1999; Zhang and Dong, 2004; Kiladis et al., 2005; Majda et al.,
58 2007; Thual et al., 2014). Observations have shown that the moist boundary layer
59 gradually deepens at the east of the MJO convection center (Johnson et al., 1999; Tian et
60 al., 2006), which is thought to be critical for the MJO's typical eastward propagation
61 speeds (Wang et al., 2018). By using reanalysis data, Hsu and Li (2012) argued that the
62 zonal asymmetry of low-level moisture relative to the MJO convection center favors the
63 eastward propagation of MJO by potentially causing a more unstable stratification on the
64 east of MJO convection center. Using a theoretical model, Wang et al. (2016a) pointed
65 out that the MJO structure is regulated by the trio-interaction among moisture, diabatic
66 heating, and large-scale dynamics. Wang and Chen (2017) addressed that the
67 asymmetries of the MJO, such as the relative intensity of low-level equatorial easterly
68 winds associated with Kelvin wave and westerly wind associated with Rossby wave,
69 strongly relate to the convective schemes. Their result shows that stronger easterly winds

70 associated with Kelvin wave produces faster eastward propagation of MJO, which is
71 consistent with other numerical results (Kang et al., 2014; Adames and Kim, 2016).

72 How about the simulation of MJO in the community of general circulation models
73 (GCMs)? Previous studies had pointed out that, although notable progresses have been
74 made, realistic simulation of the MJO is still a big challenge for many current GCMs
75 (e.g., Slingo et al., 1996; Sperber, 2004; Hung et al., 2013; Jiang et al., 2015; Ahn et al.,
76 2017). The failures related to the simulation of the MJO manifest themselves in
77 misrepresentations of the slow eastward propagating signals, seasonal cycle, spatial
78 distribution, and convective-wind coupling (Slingo et al., 1996; Sperber et al., 1997;
79 Sperber, 2004). These shortcomings are affected by cumulus parameterization (Maloney
80 and Hartmann, 2001; Peters et al., 2017), resolution (Inness et al., 2001; Liess and
81 Bengtsson, 2004; Crueger et al., 2013), mean state (Slingo et al., 1996; Inness et al.,
82 2003), and air-sea interaction (Wang and Xie, 1997; Liu and Wang, 2013; Tseng et al.,
83 2015; Fu et al., 2016, 2017). The errors introduced into GCM simulations by
84 conventional cumulus parameterization can to some extent be overcome by coupling a
85 cloud-resolving model (CRM) to GCMs at the scale of the GCM-grid to replace
86 traditional cumulus parameterization. In this methodology, referred to as
87 ‘superparameterization’, the embedded two-dimensional CRM-based convection
88 parameterization interacts with the GCM’s large-scale dynamics and has the ability to
89 enable the simulation of MJO-like signals in idealized models (Grabowski, 2001, 2003),
90 GCMs (Randall et al., 2003; Arnold et al., 2015; Wang et al., 2016b) and numerical
91 weather prediction models (Subramanian and Palmer, 2017). Instead of having to relying
92 on a cumulus convection parameterization, Miura et al. (2007) used the global CRM

93 NICAM (Nonhydrostatic Icosahedral Atmosphere Model; Satoh et al., 2008), and
94 successfully simulated the slowly eastward propagation of the MJO. Moreover, NICAM
95 has the ability to predict MJO events with lead times of up to one month with realistic
96 initial conditions (Miura et al., 2007; Miyakawa et al., 2014). The history and recent
97 developments of CRM are reviewed by Guichard and Couvreux (2017). However,
98 running a global CRM or superparameterized model is a computationally demanding
99 approach, possibly limiting its applicability in global earth system models (ESMs) used
100 for very long integrations.

101 Another approach to resolving the abovementioned issues of operational convection
102 parameterization schemes presents itself in the Stochastic Multicloud Model (SMCM)
103 Khouider et al., 2010), which is derived from the multicloud model of Khouider and
104 Majda (2006a, 2006b), and its coupling to existing convection parameterizations in
105 GCMs. The SMCM evolved out of the multicloud models introduced in Majda et al.
106 (2007) and Khouider and Majda (2008a,b) and predicts, constrained by the background
107 atmospheric state, the evolution of a cloud population (congestus, deep convection and
108 stratiform) by means of a coarse-grained birth-death process evolved in time using a
109 Markov chain Monte Carlo method. Specifically, the SMCM predicts the area fraction of
110 each cloud type per GCM grid box. Since its advent, the SMCM has successfully been
111 applied to investigate tropical convective coupled equatorial waves (Frenkel et al., 2012,
112 2013), the MJO in an aquaplanet GCM (Deng et al., 2015), and the tropical intraseasonal
113 variability in the NCEP Climate Forecast System which is a state-of-the-art coupled
114 ocean-atmosphere model (Goswami et al., 2017a, 2017b, 2017c). The SMCM has also
115 been shown to adequately reproduce observed tropical convection (Peters et al., 2013).

116 Based on the latter study, Peters et al. (2017) incorporated a modified version of the
117 SMCM, i.e. tuned to observations and including an altered internal response function,
118 into ECHAM6.3 (Stevens et al., 2013), a state-of-the-art atmospheric general circulation
119 model (AGCM) used by many research groups (e.g., Cao et al., 2017). Their results had
120 shown that coupling the SMCM into ECHAM6.3 produces a better performance of MJO
121 by analyzing and comparing the Hovmöller diagram of daily mean total surface rainfall,
122 wavenumber-frequency-spectra of outgoing longwave radiation (OLR), multivariate EOF
123 analysis (Waliser et al., 2009) and the life cycle of MJO. However, these analyses do not
124 cover all aspects related to MJO-evaluation in GCMs. In order to completely evaluate the
125 influence of SMCM on the simulation of MJO in ECHAM6.3, a set of dynamics-oriented
126 metrics proposed by Wang et al. (2018), which complements the standardized set of
127 diagnostics of the U.S. CLIVAR MJO Working Group, are applied in this study. These
128 dynamics-oriented metrics are designed to judge whether a GCM captures the eastward
129 propagation of MJO in accordance with reasonable physical processes.

130

131 **2. Model description, experiment designs, and data**

132 The subversion of ECHAM6.3 used in this study is ECHAM6.3.02 versus
133 ECHAM6.3.01p3 used in Peters et al. (2017). ECHAM6.3.02 is the atmospheric
134 component of the third generation of the Nanjing University of Information Science and
135 Technology Earth System Model (NESM3.0; Cao et al., 2017) and is the basis for the
136 atmospheric component of MPI-ESM1.2 of the Max-Planck-Institute for Meteorology
137 (Mauritsen et al., 2019). A mass flux scheme (Tiedtke, 1989) with the modification of
138 penetrative convection (Nordeng, 1994) is used for the cumulus parameterization in

139 ECHAM6.3 (see Möbis and Stevens (2012) and Stevens et al. (2013) for an overview and
140 Peters et al. (2017) for a detailed analysis of simulated convection). Coupling the SMCM
141 to ECHAM6.3's convection scheme modifies the schemes' deep-shallow trigger and
142 closure formulation according to the area fraction of deep convective clouds predicted by
143 SMCM while retaining the full interactivity of the convection with the remaining model
144 dynamics and physics. Following Peters et al. (2017), in this study, only the modification
145 of deep convection is invoked when SMCM predicts the area fraction of deep cloud is
146 larger than zero; otherwise the shallow convection is enforced in the default convection
147 parameterization (see the Appendix for a brief review). We have confirmed that salient
148 features of the SMCM-implementation shown in Peters et al. (2017), e.g. the improved
149 spatiotemporal coherence of tropical surface precipitation, are also present in this slightly
150 different model version (not shown).

151 We chose to not to use the SMCM-predicted congestus and stratiform cloud fractions
152 in our implementation as this would require a major reformulation of ECHAM's mass-
153 flux convection and large-scale cloud schemes. This is out of scope in the context of this
154 work. A different implementation of the SMCM into a comprehensive GCM (CFSv2,
155 Goswami et al. (2017a, 2017b, 2017c)) took a more rigorous approach by removing the
156 host model's mass-flux convection scheme and using prescribe heating and moistening
157 profiles for all SMCM-simulated cloud types, thereby circumventing the need to account
158 for adopting the mass-flux framework to accommodate multiple cloud types. The heating
159 and moistening profiles used in that implementation scale linearly with cloud area
160 fractions.

161 We perform AMIP-type simulations at two different resolutions (T31L47 and T63L47)

162 with the default ECHAM6.3 (named as ECHAM_CTRL), and the ECHAM6.3 coupled
163 SMCM (named as ECHAM_SMCM). The horizontal resolution of T63 (T31) is about 1.9
164 $^{\circ} \times 1.9^{\circ}$ ($3.875^{\circ} \times 3.875^{\circ}$) and vertical resolution is 47 levels extending from the surface to
165 0.01 hPa. The AMIP-type experiment integrates from 1976 to 2014 with the forcings and
166 boundary data from Coupled Model Intercomparison Project phase 6 (CMIP6). The first
167 three years are considered as spin-up phase. To keep the description and comparison
168 concise, only the results of T31L47 are discussed in this study, aiming to illustrate that
169 the SMCM also has positive influence on even coarser resolution than T63L47 (as shown
170 in Peters et al., 2017). The results of SMCM at T63L47 resolution are summarized in
171 Table 1 for completeness.

172 To evaluate the performance of the simulated MJO, the model results of CTRL and
173 SMCM are separately compared with observations. We use daily precipitation data from
174 Global Precipitation Climatology Project version 1.2 (GPCP; Huffman and Bolvin, 2013)
175 as reference, which is downloaded from <ftp://meso.gsfc.noaa.gov/pub/1dd-v1.2>. On the
176 other hand, winds, air temperature, diabatic heating, and specific humidity data are
177 obtained from ERA-Interim reanalysis (Dee et al., 2011). The reference datasets span the
178 period of 1997-2013. To make the model intrinsically represent the MJO variability and
179 to adequately explore the key processes relevant for simulation of the MJO, the whole
180 model period data (from 1979 to 2014) are used in this study. Moreover, all observations
181 are interpolated to model grids to make direct comparison between observations and
182 model results. Prior to analysis, a band-pass (20-70 days) filter is applied to all variables.
183 Then the resulting intraseasonal anomalies are analyzed for boreal winter only
184 (November to April). Six dynamics-oriented diagnoses of Wang et al. (2018) are

185 discussed:

- 186 (1) lag-longitude regression of 925 hPa boundary layer moisture convergence
- 187 (BLMC),
- 188 (2) zonal asymmetry of 850 hPa wind fields,
- 189 (3) zonal-vertical structure of equivalent potential temperature (EPT) and convective
- 190 instability index,
- 191 (4) vertical structure of diabatic heating along the equator,
- 192 (5) horizontal structure of 200 hPa divergence and 300 hPa diabatic heating,
- 193 (6) and vertical structure of available potential energy (APE) generation along the
- 194 equator.

195

196 Two studying areas are chosen: one is in the eastern Indian Ocean (EIO) and the other
197 is in the western Pacific Ocean (WPO). To demonstrate and emphasize the planetary
198 scale of the MJO, we consider relatively large studying areas (EIO: 10°S-10°N; 80-100°E,
199 WPO: 10°S-10°N; 130-160°E). Note that the results discussed in this study are relative to
200 EIO unless stated otherwise.

201

202 **3. Results**

203 **3.1 Annual mean precipitation**

204 Implementation of the SMCM into ECHAM6.3 results in an imbalance in the top-of-
205 the atmosphere (TOA) radiation budget. Peters et al. (2017) noted this, but did not
206 perform a retuning of the model. The model version used here was retuned in order to
207 maintain TOA radiation balance – mainly through parameters related to clouds (see

208 Mauritsen et al. 2012 for details regarding the tuning of ECHAM6). The impacts of
209 SMCM on global energy balance, global water balance, and the tuning processes are
210 summarized in another work (in preparation). The annual mean precipitation is briefly
211 discussed here. Compared to the global annual mean of GPCP (2.68 mm/day), model
212 results show larger global annual mean precipitation rate. They are 2.94 mm/day, 2.90
213 mm/day, and 2.86 mm/day for ECHAM_CTRL, ECHAM_SMCM_ORI, and
214 ECHAM_SMCM, respectively. Here ECHAM_SMCM_ORI represents the version
215 ECHAM6.3 coupling SMCM with default parameters as ECHAM_CTRL.
216 ECHAM_SMCM represents the retuned version of ECHAM6.3 which includes the
217 SMCM. The three model versions produce similar geographic distribution of annual
218 mean precipitation (pattern correlation coefficient (PCC), which is calculated between
219 model simulation and observation, is 0.84 for the three model simulations). But
220 ECHAM_SMCM_ORI and ECHAM_SMCM have larger root-mean square error than
221 that of ECHAM_CTRL, which is 1.15 mm/day versus 1.07 mm/day.

222 Recalling the results shown by Peters et al. (2017), ECHAM_SMCM_ORI reduces the
223 precipitation amount over land, especially over South America. Figure 1 depicts the
224 difference among model results and observation. It shows that ECHAM_SMCM and
225 ECHAM_SMCM_ORI have similar bias pattern (Fig. 1a,b). However, the retuning
226 results in systematic increase of precipitation over land and the maritime continent,
227 thereby reducing the dry biases compared to observations when using an untuned model
228 version (Fig. 1a and Peters et al. 2017). At the same time, the precipitation distribution
229 over the tropical Atlantic is improved by significantly reducing the overestimation of
230 precipitation near the South American coast. The overestimation of precipitation in the

231 South Pacific Convergence Zone seen in ECHAM_SMCM_ORI (Fig. 1a) is also reduced
232 in ECHAM_SMCM (Fig. 1b,c). Thus, the following discussion focuses on the
233 comparison between ECHAM_SMCM and ECHAM_CTRL.

234

235 **3.2 Impact of SMCM on the eastward propagation of the MJO**

236 The MJO most prominently manifests itself in a slowly eastward propagating envelope
237 of organized deep convection which is also key to its life cycle (Madden and Julian,
238 1972). Thus, before exploring the influence of the SMCM on MJO through the dynamics-
239 oriented metrics, the impact of the SMCM on the eastward propagation of the MJO in
240 ECHAM6.3 is firstly discussed here. Here the eastward propagation of the MJO is
241 straightforwardly depicted by the lag-longitude correlation of precipitation anomalies
242 (Waliser et al., 2009). That is the averaged precipitation within the reference region (EIO
243 or WPO) and 20-70 day filtered daily precipitation are used to conduct the lag-longitude
244 correlation analysis.

245 Lag-longitude correlation maps of observed precipitation show that the MJO
246 continuously propagates eastward from 50°E to 180°E referred to the precipitation in the
247 EIO (Fig.2a; e.g., Jiang et al., 2015; Wang et al., 2018). In ECHAM_CTRL, westward
248 propagating precipitation is simulated (Fig. 2b). ECHAM_SMCM shows eastward
249 propagating precipitation anomalies from 50°E to 140°E, indicating the presence of a
250 simulated MJO-like disturbance. Although ECHAM_SMCM significantly improves the
251 behavior of the eastward propagation of organized precipitation, i.e. the MJO, compared
252 to ECHAM_CTRL (cf. Peters et al. 2017), it fails to capture the zonal extension of the
253 propagation compared to observations (Fig. 2c). Using a different SMCM-

254 implementation approach into a comprehensive GCM, Goswami et al. (2017c) found
255 similar results (Fig. 4 in Goswami et al. (2017c)). Further, the reader is referred to the
256 analysis of standard MJO diagnostics presented in Peters et al. (2017) indicating that the
257 performance of our implementation is comparable to other, more direct implementations
258 of the SMCM in comprehensive GCM frameworks (i.e., Goswami et al., 2017a, 2017b,
259 2017c).

260 To measure the performance of the simulated MJO in ECHAM_SMCM, the pattern
261 correlation coefficient (PCC) and normalized root mean square error (NRMSE) between
262 observations and model results are calculated. Here the NRMSE is the RMSE between
263 observations and model results normalized by observations' standard deviation. As
264 revealed by observation and model results, a local stationary oscillation of MJO in the
265 EIO mainly centers at the longitudinal range from 85°E to 95°E (e.g., Jiang et al., 2015;
266 Wang and Lee, 2017). Thus to eliminate the stationary behavior of MJO, the PCC and
267 NRMSE are calculated within the time-longitude domain (50-180°E, from day -20 to day
268 20) where the absolute correlation coefficient is larger than 0.2 and within ± 20 days in
269 the observation, by excluding the longitude range from 85°E to 95°E (Wang et al., 2018).
270 Due to the westward propagation of MJO, ECHAM_CTRL has a very low PCC and large
271 NRMSE, which are 0.14 and 1.02, respectively (Table 1). Consistent with the results
272 shown by the lag-longitude correlation map, ECHAM_SMCM has much better PCC
273 (0.76) and NRMSE (0.62) scores (Table 1).

274 Besides comparison of the eastward propagation of MJO in the EIO, we also analyzed
275 the propagation of the MJO in the WPO. Similar to the performance of MJO in EIO,
276 ECHAM_SMCM shows eastward propagation of MJO in the WPO, while

277 ECHAM_CTRL simulates westward propagating precipitation anomalies (figures not
278 shown here). The PCC and NRMSE scores confirm that ECHAM_SMCM has better
279 performance than that of ECHAM_CTRL. As listed in Table 1, the PCC and NRMSE of
280 ECHAM_SMCM (ECHAM_CTRL) are 0.82 (0.68) and 0.54 (0.67), respectively. The
281 results are similar for T63L47 resolution (Table 1).

282

283 **3.3 Dynamics-oriented diagnostic metrics**

284 In this section, the impact of SMCM on the performance of simulated MJO is explored
285 through the dynamics-oriented diagnostics proposed by Wang et al. (2018).

286

287 **3.3.1 Boundary layer moisture convergence**

288 Observational evidence and model results have shown that the boundary layer
289 convergence may be a crucial factor determining the eastward propagation of the MJO
290 (e.g., Maloney and Hartmann, 1998; Wang et al., 2016; Wang and Lee, 2017). Figure 3
291 depicts the propagation of BLMC at 925 hPa in the EIO. Similar to the propagation of
292 precipitation, observations show that the BLMC-signal systematically propagates
293 eastward from 50°E to 180°E (Fig. 3a). BLMC as simulated by ECHAM_CTRL
294 (ECHAM_SMCM) propagates westward and eastward, respectively (Figs. 3b and 3c),
295 comparing well to the propagation of precipitation anomalies in the simulations (Fig.
296 2b,c). The PCC and NRMSE scores support the impression gained from Fig. 3 and
297 confirm that SMCM T31L47 performs better than CTRL T31L47 in terms of the
298 propagation of BLMC associated with the MJO. The results are similar when using the
299 WPO as reference region. The comparison addressed here supports the view of a better

300 performance of propagation of BLMC reproduces realistic and better eastward
301 propagation of MJO in precipitation in the EIO and WPO (e.g., Wang et al., 2018). One
302 would think that this should naturally be the case because organized precipitation in the
303 tropics is associated with low-level convergence. So nothing is really new here. However,
304 this has been already found in previous studies that convection schemes often miss a link
305 to large-scale dynamics and are closed on local thermodynamic quantities, e.g.
306 convective available potential energy (CAPE). This is not the case for the
307 ECHAM_SMCM, which by implementation is coupled to large-scale dynamics at 500
308 hPa, explaining its superior performance compared to ECHAM_CTRL.

309

310 **3.3.2 850 hPa horizontal circulation**

311 The propagation of the MJO is closely related to the low-level wind circulation (Wang
312 and Lee, 2017) and intrinsically associated with the zonal extent and strength of Kelvin
313 and Rossby waves (Gill, 1980; Kang et al., 2014; Adames and Kim, 2016; Wang et al.,
314 2016; Wang and Chen, 2017). Figure 4a shows the horizontal circulation as obtained
315 from re-analyses at 850 hPa. It shows zonal asymmetry with westerlies and easterlies at
316 the west and east of the major convection center, respectively. Both model results have
317 the similar feature of zonal asymmetry (Figs. 4b and 4c). However, there are some
318 differences between the observation and model results. Compared to observations, both
319 model results have westward center of the Kelvin wave-induced easterly. And the center
320 of the Kelvin wave-induced easterly of model results locates at the southern side of
321 equator, while the center of the Kelvin wave-induced easterly in observation appears at
322 the north of equator. Figure 4d shows the meridional average of the zonal wind in the

323 latitudinal range from 5°S to 5°N. ECHAM_SMCM has the same zonal extent ratio
324 between the Kelvin wave-induced easterly and the Rossby wave-induced westerly (K-R),
325 which is about 2.1, with that of observation. The zonal extent ratio of K-R of
326 ECHAM_CTRL is only about 1.0. On the other hand, although ECHAM_SMCM has
327 comparable zonal extent ratio of K-R, it has larger R-K intensity ratio, which is measured
328 by the maximum speed of Rossby wave-induced westerly versus that of Kelvin wave-
329 induced easterly. The R-K intensity ratio of observation and ECHAM_SMCM are 0.8 and
330 1.4, respectively. Moreover, the R-K intensity ratio of ECHAM_CTRL is about 1.8. The
331 superior performance of ECHAM_SMCM compared to ECHAM_CTRL in terms of
332 capturing the MJO associated low-level circulation is also confirmed by the PCC and
333 NRMSE scores (Table 1).

334

335 **3.3.3 Equivalent Potential Temperature structure**

336 Figure 5 shows the structures of equivalent potential temperature (EPT) anomalies,
337 which are the meridional average between 5°S and 5°N. The maximum of EPT anomalies
338 of observations and both model results are found at 500 hPa. Similar to the characteristics
339 seen in observations, ECHAM_SMCM successfully models the tilted structure of EPT
340 (Figs. 5a and 5c). From low-level to the height at 500 hPa, the EPT of ECHAM_SMCM
341 illustrates a westward and upward (rearward) tilted structure. Then a reverse tilted
342 structure, which is eastward and upward, in the upper troposphere above 400 hPa. The
343 low-level rearward tilt favors a gradual deepening of the moist layer and moves westward
344 relative to the major convection center and is thought to stimulate the eastward
345 propagation of MJO (e.g., Jiang et al., 2015). ECHAM_CTRL on the other hand does not

346 indicate any tilted structure (Fig. 5b). As suggested by previous studies (e.g., Li and Hsu,
347 2012; Wang and Lee, 2017; Wang et al., 2018), we apply a convective instability index to
348 measure the conditions of destabilization of the atmospheric column with respect to deep
349 convection to the east of major convection center. To this end, the difference of EPT
350 between 850 hPa and 400 hPa (850 hPa EPT minus 400 hPa EPT; Fig. 5d) is firstly
351 calculated. Then the convective instability index is calculated by averaging the previously
352 computed difference in the longitudinal range from 120°E to 150°E. The convective
353 instability indices of observation, ECHAM_CTRL, and ECHAM_SMCM are 0.39, 0.20,
354 and 0.34, respectively, implying that ECHAM_SMCM captures the observed generation
355 of high convective instability to the east of MJO convection center, but ECHAM_CTRL
356 fails to do so. Moreover, ECHAM_SMCM simulates the zonal asymmetry well (Fig. 5d).
357 This improvement of ECHAM_SMCM is probably realized in terms of the modification
358 of the deep-convective trigger. Recall that Peters et al. (2017) showed that this SMCM
359 implementation into ECHAM6.3 leads to an increased number of shallow convective
360 events reaching deeper into the atmosphere- mimicking the effect of congestus cloud on -
361 potentially acting to precondition the atmosphere with regards to the occurrence of deep
362 convection. The improvement of ECHAM_SMCM is also manifested by the PCC and
363 NRMSE scores of EPT anomaly profiles, which are 0.87 and 0.76 versus 0.66 and 1.01 of
364 ECHAM_CTRL, respectively (Table 1).

365

366 **3.3.4 Vertical structure of diabatic heating**

367 As shown in Fig. 6a, there is rearward (westward) tilted structure in the lower
368 troposphere of the diabatic heating as represented in the reanalysis, reminiscent of the

369 deepening of convection as the MJO-envelope propagates eastward. Note that vertical
370 structures of diabatic heating of observation and model simulation shown in Fig. 6 are
371 calculated by the meridional average between 5°S and 5°N. However, there is no such
372 tilted structure simulated by ECHAM_CTRL (Fig. 6b), implying that ECHAM_CTRL
373 probably fails to simulate the observed transition of cloud types, such as the transition
374 from clear sky to congestus and shallow and congestus clouds to deep convective cloud.
375 Although it is not as obvious as in the observations, ECHAM_SMCM successfully
376 models the rearward tilted structure in the lower troposphere (Fig. 6c). Both model results
377 depict a narrowly trapped structure of diabatic heating compared to that of the reanalysis
378 and demonstrate stronger diabatic heating. The ameliorated capacity of ECHAM_SMCM
379 to simulate the zonal asymmetry of equatorial diabatic heating is confirmed by the PCC
380 and NMRSE values (Table 1).

381

382 **3.3.5. Upper-level divergence**

383 Similar to the low-level horizontal divergence, the distribution of upper-level horizontal
384 divergence can also be used to monitor the eastward propagation of MJO (Adames and
385 Wallace, 2014). Figure 7 shows the horizontal distributions of winds and divergence at
386 200 hPa and the diabatic heating at 300 hPa. The observed upper-level circulation
387 (vectors in Fig. 7a), which consists of the equatorial easterlies at the west of convective
388 center and the equatorial westerlies at the east of convective center, shows the
389 approximately out-of-phase relationship to that at 850 hPa (vectors in Fig. 4a) (Wheeler
390 and Hendon, 2004; Waliser et al., 2009). The 200 hPa divergence is closely associated
391 with the 300 hPa diabatic heating. Compared to the model result shown by

392 ECHAM_CTRL (Fig. 7b), ECHAM_SMCM largely simulates the observed 200 hPa
393 wind pattern accompanying the westerlies at the east of convection center and easterlies
394 at the west of convection center (Fig. 7c). However, there are some shortcomings. Like
395 ECHAM_CTRL, there is no western extension of 200 hPa divergence and 300 hPa
396 diabatic heating, instead the 200 hPa divergence extends northeastward. Moreover,
397 ECHAM_SMCM also shows stronger convergence at the east of convection center than
398 the reanalyses. The PCC and NRMSE of 200 hPa divergence and 300 hPa diabatic
399 heating are calculated in the domain enclosed by black box (50-160°E and 15°S-15°N).
400 As to 200 hPa divergence, the PCC and NRMSE of ECHAM_SMCM (EHCAM_CTRL)
401 are 0.78 (0.68) and 1.09 (1.53), respectively. ECHAM_SMCM also outperforms
402 ECHAM_CTRL with regards to 300 hPa diabatic heating (Table 1).

403

404 **3.3.6. Vertical distribution of available potential energy**

405 Figure 8 displays the generation rate of vertical equatorial APE from 40°E to 180°E.
406 As reported by other studies (e.g., Wang and Lee, 2017; Wang et al., 2018), the observed
407 APE generation rate exhibits significant zonal asymmetry relative to the MJO convection
408 center in the lower troposphere (Fig. 8a). The generation rate of MJO APE at the east of
409 90°E is larger than the one at the west of 90°E. As to the model results, both of them are
410 capable of simulating the maximum center of APE generation rate at the upper
411 troposphere as observation (Figs. 8b and 8c). However, both model results have poor
412 simulation in the middle and lower troposphere (below 450 hPa) compared to
413 observations. As shown in Fig. 8b, ECHAM_CTRL shows an interruption of APE
414 generation rate in the middle troposphere over the MJO convection center. After the

415 modification of deep convection trigger through the SMCM-implementation,
416 ECHAM_SMCM is able to better represent the MJO APE generation rate at the east of
417 the MJO convection center (Fig. 8c). But ECHAM_SMCM still fails to capture the
418 observed vertical structure at the west of 90°E in the middle and lower troposphere.
419 Furthermore, the PCC and NRMSE between simulated and observed APE generation rate
420 calculated in the domain (40-180°E and 1000-200 hPa) are used to measure the
421 performance of simulations. The PCC and NRMSE of ECHAM_SMCM
422 (ECHAM_CTRL) are 0.55 (0.40) and 1.17 (1.11), respectively.

423

424 **4. Conclusions and discussion**

425 As the preceding work of Peters et al. (2017), the influence of the SMCM on the
426 capacity of the state-of-the-art GCM ECHAM6.3 to simulate the MJO is further
427 evaluated in this study. Contrary to the model version discussed in Peters et al. (2017),
428 the model used here was retuned to maintain top-of-the-atmosphere radiation balance.
429 This retuning significantly reduces the precipitation biases over tropical land masses
430 reported in Peters et al. (2017). Furthermore model simulations at two different horizontal
431 resolutions, T31 and T63, are analyzed here, with both setups having the same amount of
432 vertical levels (47). Analysis of lag-longitude correlation maps of precipitation in the East
433 Indian Ocean (EIO) and the West Pacific Ocean (WPO) clearly show that the SMCM-
434 implementation results in the simulation of an MJO, whereas the standard model version
435 cannot do so, thus confirming the results of Peters et al. (2017). Extending on the analysis
436 of Peters et al. (2017), the influence of the SMCM-implementation on MJO-dynamics is
437 analyzed by applying six dynamics-oriented diagnostic metrics proposed by Wang et al.

438 (2018).

439 The six dynamics-oriented metrics are (1) lag-longitude correlation of BLMC, (2)
440 zonal asymmetry of low-level circulation (850 hPa), (3) vertical structure of the EPT and
441 convective instability, (4) zonally asymmetric distribution of vertical diabatic heating, (5)
442 zonal asymmetry of the upper-level divergence (200 hPa) and diabatic heating (300 hPa),
443 and (6) generation of the MJO APE. Measured by PCCs and NRMSEs, it is obvious that
444 ECHAM_SMCM outperforms the ECHAM_CTRL in terms of the first five dynamics-
445 oriented metrics (Table 1). Especially, the benefits obtained by ECHAM_SMCM are
446 clear by comparing the lag-longitude correlation of BLMC, zonal asymmetry of low- and
447 upper-level circulation, the vertical structure of the EPT and convective instability, and
448 zonal asymmetry of vertical diabatic heating; whereas it is less clear in others.
449 ECHAM_SMCM successfully simulates the observed eastward propagation of the
450 BLMC, the observed tilted structure of vertical EPT and diabatic heating along equator.
451 In terms of the horizontal circulation at 850 hPa, compared to ECHAM_CTRL,
452 ECHAM_SMCM has stronger Kelvin easterlies at the east of MJO convection center and
453 smaller R-K intensity ratio, which is thought to favor the eastward propagation of MJO
454 (e.g., Kang et al., 2014; Wang and Chen, 2017). By comparing the 200 hPa winds,
455 ECHAM_SMCM captures the observed features, depicting Rossby easterlies at the west
456 and Kelvin westerlies at the east of convection center.

457 By coupling of the model SMCM into ECHAM6.3, only the trigger of deep convection
458 and its closure, which is predicted by the model SMCM, is modified (Peters et al., 2017).
459 This reformulation of the occurrence and strength of deep convection allows it to
460 organize more realistically and thus couple more effectively to the large-scale dynamics,

461 eventually resulting in the simulation of the MJO. Although coupling the SMCM into
462 ECHAM6.3 improves the performance of simulated MJO in this study, there is still a
463 long way to go to simulate it perfectly, such as the MJO's APE generation rate. Previous
464 studies suggested that the shallow convection may exert significant influence on the
465 simulation of the MJO (e.g., Thayer-Calder and Randall, 2009; Tseng et al., 2015; Hirota
466 et al., 2018). Additionally, congestus and stratiform cloud heating, which was first
467 thoroughly studied in Majda and Shefter (2001) and takes part in the conception of the
468 multcloud model (Khouider and Majda, 2006a), has been shown to play a vital role in
469 the growth and propagation of the MJO (e.g., Mapes, 2000; Kuang, 2008; Fu and Wang,
470 2009). Both aspects are not covered by the SMCM implementation discussed here – there
471 are noticeable impacts on the simulation of shallow convection (Peters et al., 2017).

472 In fact, the SMCM predicts the temporal evolution of three cloud types: congestus,
473 deep convective and stratiform clouds (Khouider et al., 2010). Linearly scaled heating
474 and moistening profiles of all three cloud types have been used for a more rigorous
475 implementation of the SMCM into a comprehensive GCM (CFSv2, Goswami et al.
476 (2017a, 2017b, 2017c)) which leads to ameliorated performance of that model in the
477 simulation of synoptic and intraseasonal variability in the tropics. However, the analysis
478 presented here, in support of Peters et al. (2017), shows that the SMCM also has the
479 potential to provide the backbone of a new generation mass-flux convection scheme
480 calculating the occurrence of multiple convective clouds/updrafts alongside each other
481 for use in GCMs – the benefit of which would be a complete integration into the host
482 model's dynamics and physics.

483 The question then arising is: Is it possible to further improve the performance of

484 simulated MJO by fully coupling the SMCM into ECHAM6.3 or any other existing state-
485 of-the-art GCM using the convective mass-flux approach? Given the results presented
486 here and in previous studies, that question is worth investigating through investments in
487 thorough model development in the future.

488

489 **Acknowledgements**

490 We thank Dr. Thorsten Mauritsen from Max-Planck-Institute for Meteorology on the
491 suggestion of tuning the TOA imbalance. This work is supported by the National Key
492 R&D Program of China (Grant No. 2018YFC1505803). This study is also sponsored by
493 the Nanjing University of Information Science and Technology through funding the joint
494 China-US Atmosphere-Ocean Research Center at the University of Hawaii at Manoa, and
495 the Startup Foundation for Introducing Talent of NUIST (No. 2018r064). KP
496 acknowledges funding by the Deutscher Wetterdienst (DWD) within the Hans-Ertel-
497 Zentrum for Weather Research (HErZ). This is the IPRC publication number 1385 and
498 the ESMC publication number 260.

499

500 **Appendix**

501 The incorporation of SMCM into ECHAM6.3 and the effects of SMCM on the
502 convection are briefly described in this appendix. Readers can refer to Peters et al. (2017)
503 for the details of the implementation of SMCM into ECHAM6.3.

504 To overcome the underestimation (overestimation) of convection for strong (weak)
505 large-scale forcing, Peters et al. (2017) adopted a modified SMCM. In modified SMCM,
506 they replaced a function relating to the transition rate between different cloud types. The

507 transition rate is exerted by the atmospheric large-scale state. The original function
 508 related to the transition rate (Khouider et al., 2010) has the following form:

$$509 \quad \Gamma_1(x) = 1 - e^{-x}, \quad x \in [0, 2], \quad (\text{A1})$$

510 where x is C or D . C and D , which are the proxies for initiating and sustaining the deep
 511 convection and for midtropospheric dryness inhibiting the deep convection, respectively,
 512 are the two variables in the SMCM (Peters et al., 2013). Thus the transition rate can be
 513 formulated as $R_{ab} \propto \Gamma_1(C)\Gamma_1(D)$. Peters et al. (2013) pointed out the equation (A1)
 514 related R_{ab} misrepresents the convective activity, which underestimates the convection
 515 for strong large-scale forcing and overestimates the convection for weak large-scale
 516 forcing. In Peters et al. (2017), they applied to a *tanh*-related formulation:

$$517 \quad \Gamma_2(x) = 0.52 \left(0.964 + \tanh(2(x-1)) \right), \quad x \in [0, 2]. \quad (\text{A2})$$

518 This modification makes SMCM run have the adequate ability to simulate the observed
 519 behavior of convection (e.g., Peters et al., 2013).

520 The SMCM used in Peters et al. (2017) and in this study aims to predict the base mass
 521 flux of the deep convective cloud. The base mass flux M_{cb} of deep-convection cloud is
 522 formulated as:

$$523 \quad M_{cb} = \sigma_d w_{cb} \rho_{cb}, \quad (\text{A3})$$

524 where σ_d is the area fraction of deep convection; w_{cb} and ρ_{cb} are the vertical upward
 525 velocity and the air density at cloud base, respectively. With the large-scale state variables
 526 relative humidity and vertical pressure velocity at around 500 hPa, SMCM intends to
 527 predict σ_d . Combined with default convective scheme used in ECHAM6.3, SMCM
 528 modifies the deep-shallow-convection trigger. If the convection is diagnosed and the

529 predicted $\sigma_d > 0$, then the deep convection is performed. If the convection scheme is
530 invoked and $\sigma_d = 0$, then the shallow convection is performed.

531 How does the SMCM affect the convection? In-depth analysis by Peters et al. (2017)
532 pointed out that the SMCM adopted in ECHAM6.3 improves (a) moisture-convection
533 coupling, (b) spatiotemporal coherence of tropical daily rainfall, (c) representation of
534 M_{cb} , (d) enhanced covariance of large-scale and convective precipitation, and (e) more
535 continuity of subdaily deep convection. On the other hand, the SMCM suppresses the
536 occurrence of deep convection at the places where do not support the deep convection.
537 This leads to ECHAM6.3 coupled with SMCM produces more realistic spatiotemporal
538 coherence of daily rainfall at tropics. The improved spatiotemporal coherence of daily
539 rainfall enhances the model capacity to simulate the MJO.

540

541 **References**

542 Adames, A. F., and D. Kim, 2016. The MJO as a dispersive, convectively coupled
543 moisture wave: Theory and observations. *J. Atmos. Sci.*, 73: 913-914.

544 Adames, A. F., and J. M. Wallace. 2014. Three-dimensional structure and evolution of
545 the vertical velocity and divergence fields in the MJO. *J. Atmos. Sci.*, 71: 4661-4681.

546 Ahn, M. S., D. Kim, K. Sperber, E. Maloney, et al. 2017. MJO simulation in CMIP5
547 climate models: MJO skill metrics and process-oriented diagnosis. *Clim. Dyn.*, 49:
548 4023-4049.

549 Arnold, N. P., M. Branson, Z. M. Kuang, D. A. Randall, and E. Tziperman. 2015. MJO
550 intensification with warming in the superparameterized CESM. *J. Clim.*, 28: 2706-
551 2724.

552 Cao, J., B. Wang, Y.-M. Yang, L. B. Ma, et al. 2017. The NUIST earth system model
553 (NESM) version 3: Description and preliminary evaluation. *Geosci. Model Dev.*,
554 Discussion, <https://doi.org/10.5194/gmd-2017-206>.

555 Crueger, T., B. Stevens, and R. Brokopf. 2013. The Madden-Julian oscillation in
556 ECHAM6 and the introduction of an objective MJO metric. *J. Clim.*, 26: 3241-3257.

557 DeMott, C. A., N. P. Klingaman, and S. J. Woolnough. 2015. Atmosphere-ocean coupled
558 processes in the Madden-Julian Oscillation. *Reviews of Geophys.*, 53: 1099-1154.

559 Dee, D. P., et al. 2011. The ERA-interim reanalysis: configuration and performance of the
560 data assimilation system. *Quart. J. Roy. Meteorol. Soc.*, 137: 553-597.

561 Deng, Q., B. Khouider, and A. J. Majda. 2015. The MJO in a coarse-resolution GCM
562 with a stochastic multcloud parameterization. *J. Atmos. Sci.*, 72: 55-74.

563 Deng, Q., B. Khouider, A.J. Majda, and R.S. Ajayamohan, 2016: Effect of
564 StratiformHeating on the Planetary-Scale Organization of Tropical Convection. *J.*
565 *Atmos. Sci.*,73, 371–392.

566 Frenkel, Y., A. J. Majda, and B. Khouider. 2012. Using the stochastic multcloud model to
567 improve tropical convective parameterization: A paradigm example. *J. Atmos. Sci.*, 69:
568 1080-1105.

569 Frenkel, Y., A. J. Majda, and B. Khouider. 2013. Stochastic and deterministic multcloud
570 parameterizations for tropical convection. *Clim. Dyn.*, 41: 1527-1551.

571 Fu, X. H., and B. Wang. 2009. Critical roles of the stratiform rainfall in sustaining the
572 Madden-Julian oscillation: GCM experiments. *J. Clim.*, 22: 3939-3959.

573 Fu, X. H., W. Q. Wang, J.-Y. Lee, B. Wang, K. Kikuchi, J. W. Xu, J. Li, and S. Weaver.
574 2016. Distinctive roles of air-sea coupling on different MJO events: A new perspective

575 revealed from the DYNAMO/CINDY Field campaign. *Monthly Weather Review*, 143:
576 794-812.

577 Fu, X. H., W. Q. Wang, T. Shinoda, H. L. Ren, and X. L. Jia. 2017. Toward understanding
578 the diverse impacts of air-sea interaction on MJO simulations. *J. Geophys. Res. Oceans*,
579 122: 8855-8875.

580 Gill, A. E. 1980. Some simple solutions for heat-induced tropical circulation. *Quart. J.*
581 *Roy. Meteorol. Soc.*, 106: 447-462.

582 Grabowski, W. W. 2001. Coupling cloud processes with the large-scale dynamics using
583 the cloud-resolving convection parameterization (CRCP). *J. Atmos. Sci.*, 58: 978-997.

584 Grabowski, W. W. 2003. MJO-like coherent structure: sensitivity simulations using the
585 cloud-resolving convection parameterization (CRCP). *J. Atmos. Sci.*, 60: 847-864.

586 Goswami, B. B., B. Khouider, R. Phani, P. Mukhopadhyay, and A. J. Majda. 2017a.
587 Implementation and calibration of a stochastic multicloud convective parameterization
588 in the NCEP climate forecast system (CFSv2). *J. Adv. Model. Earth Syst.*, 9: 1721-
589 1739.

590 Goswami, B. B., B. Khouider, R. Phani, P. Mukhopadhyay, and A. J. Majda, 2017b.
591 Improved tropical modes of variability in the NCEP climate forecast system (Version
592 2) via a stochastic multicloud model. *J. Atmos. Sci.*, 74: 3339-3366.

593 Goswami, B. B., B. Khouider, R. Phani, P. Mukhopadhyay, and A. J. Majda, 2017c.
594 Improving synoptic and intraseasonal variability in CFSv2 via stochastic
595 representation of organized convection. *Geophys. Res. Lett.*, 44: 1104-1113.

596 Guichard, F., and F. Couvreux. 2017. A short review of numerical cloud-resolving
597 models. *Tellus A*, 69:1.

598 Hirota, N., T. Ogura, H. Tatebe, H. Shiogama, M. Kimoto, and M. Watanabe. 2018. Roles
599 of shallow convective moistening in the eastward propagation of the MJO in
600 MIROC6. *J. Clim.*, 31: 3033-3047.

601 Hsu, P.-C., and T. Li. 2012. Role of the boundary layer moisture asymmetry in causing
602 the eastward propagation of the Madden-Julian Oscillation. *J. Clim.*, 25: 4914-4931.

603 Huffman, G. J., and D. T. Bolvin. 2013. Version 1.2 GPCP one-degree daily precipitation
604 data set documentation (ftp://precip.gsfc.nasa.gov/pub/1dd-v1.2/1DD_v1.2_doc.pdf).

605 Hung, M.-P., J.-L. Lin, W. Wang, D. Kim, T. Shinoda, and S. J. Weaver. 2013. MJO and
606 convectively coupled equatorial waves simulated by CMIP5 climate models. *J. Clim.*,
607 26: 6185-6214.

608 Inness, P. M., and J. M. Slingo. 2003. Simulation of the Madden-Julian oscillation in a
609 coupled general circulation model. Part I: comparisons with observations and an
610 atmosphere-only GCM. *J. Clim.*, 16: 345-364.

611 Inness, P. M., J. M. Slingo, S. J. Woolnough, R. B. Neale, and V. D. Pope. 2001.
612 Organization of tropical convection in a GCM with varying vertical resolution:
613 Implications for the simulation of the Madden-Julian Oscillation. *Clim. Dyn.*, 17: 777-
614 793.

615 Jiang, X., D. E. Waliser, P. K. Xavier, J. Petch, et al. 2015. Vertical structure and physical
616 processes of the Madden-Julian oscillation: Exploring key model physics in climate
617 simulations. *J. Geophys. Res. Atmos.*, 120: 4718-4748.

618 Johnson, R. H., T. M. Rickenbach, S. A. Rutledge, P. E. Ciesielski, and W. H. Schubert.
619 1999. Trimodal characteristics of tropical convection. *J. Clim.*, 12: 2397-2418.

620 Kang, I. S., F. Liu, M. S. Ahn, Y. M. Yang, and B. Wang. 2014. Role of SST structure on

621 convectively coupled Kelvin-Rossby waves and its implication on MJO formation. *J.*
622 *Clim.*, 26: 5915-5930.

623 Khouider, B., J. Biello, and A. J. Majda. 2010. A stochastic multcloud models for
624 tropical convection. *Comm. Math. Sci.*, 8: 187-216.

625 Khouider, B., and A. J. Majda. 2006a. Model multi-cloud parameterizations for
626 convectively coupled waves: Detailed nonlinear wave evolution. *Dyn. Atmos.*
627 *Oceans*, 42: 59-80.

628 Khouider, B., and A. J. Majda. 2006b. A simple multcloud parameterization for
629 convectively coupled tropical waves. Part I: Linear analysis. *J. Atmos. Sci.*, 63: 1308–
630 1323.

631 Khouider, B., and A. Majda (2008a), Multicloud models for organized tropical
632 convection: Enhanced congestus heating, *J. Atmos. Sci.*, 65(3), 895–914.

633 Khouider, B., and A. J. Majda. 2008b. Equatorial convectively coupled waves in a simple
634 multcloud model. *J. Atmos. Sci.*, 65: 3376-3397.

635 Kiladis, G. N., K. H. Straub, and P. T. Haertel. 2005. Zonal and vertical structure of the
636 Madden-Julian oscillation. *J. Atmos. Sci.*, 62: 2790-2809.

637 Kuang, Z. M. 2008a. A moisture-stratiform instability for convectively coupled waves. *J.*
638 *Atmos. Sci.*, 65: 834-854.

639 Kuang, Z. M. 2008b. CORRIGENDUM. *J. Atmos. Sci.*, 65:9, 3011-3011.

640 Liess, S., and L. Bengtsson. 2004. The intraseasonal oscillation in ECHAM4 part II:
641 Sensitivity studies. *Clim. Dyn.*, 22: 671-688.

642 Liu, F., and B. Wang. 2013. An air-sea coupled Skeleton model for the Madden-Julian
643 oscillation. *J. Atmos., Sci.*, 70: 3147-3156.

644 Madden, R.A. and P. R. Julian, 1971. Detection of a 40-50 Day Oscillation in the Zonal
645 Wind in the Tropical Pacific, *J. Atmos. Sci.*, 28: 702-708.

646 Madden, R. A. and P. R. Julian, 1972. Description of global-scale circulation cells in the
647 tropics with a 40-50 day period. *J. Atmos. Sci.*, 29: 1109-1123.

648 Maloney, E. D, and D. L. Hartmann. 1998. Frictional moisture convergence in a
649 composite life cycle of the Madden-Julian oscillation. *J. Clim.*, 11: 2387-2403.

650 Maloney, E. D, and D. L. Hartmann. 2001. The sensitivity of intraseasonal variability in
651 the NCAR CCM3 to changes in convective parameterization. *J. Clim.*, 14: 2015-2034.

652 Majda, A. J., and M. Shefter, 2001b. Models for stratiform instability and convectively
653 coupled waves. *J. Atmos. Sci.*, 58, 1567–1584.

654 Majda, A. J., S. N. Stechmann, and B. Khouider, 2007. Madden-Julian Oscillation analog
655 and intraseasonal variability in a multicloudbelow the equator, *Proc. Natl.*
656 *Acad. Sci. U. S. A*, 104(24), 9919–9924, doi:10.1073/pnas.0703572104

657 Mapes, B. E. 2000. Convective inhibition, subgrid-scale triggering energy, and stratiform
658 instability in a toy tropical wave model. *J. Atmos. Sci.*, 57: 1515-1535.

659 Mauritsen, T., J. Bader, T. Becker, J. Behrens, and et al., 2019. Developments in the MPI-
660 M Earth System Model version 1.2 (MPI-ESM 1.2) and its response to increasing
661 CO₂. *J. Adv. Model. Earth Sys.*, <https://doi.org/10.1029/2018MS001400>.

662 Mauritsen, T., B. Stevens, E. Roeckner, T. Crueger, M. Esch, et al. 2012. Tuning the
663 climate of a global model. *J. Adv. Model. Earth Syst.*, 4, doi:10.1029/2012MS000154.

664 Miura, H., M. Satoh, T. Nasuno, A. T. Noda, and K. Oouchi, 2007. A Madden-Julian
665 Oscillation event simulated using a global cloud-resolving model. *Science*, 318, 1763-
666 1765.

667 Miyakawa, T., M. Satoh, H. Miura, H. Tomita, H. Yashiro, A. T. Noda, Y. Yamada, C.
668 Kodama, M. Kimoto, and K. Yoneyama, 2014: Madden-Julian Oscillation prediction
669 skill of a new-generation global model. *Nature Commun.*, 5, 3769.

670 Möbis, B., and B. Stevens. 2012. Factors controlling the position of the intertropical
671 convergence zone on an aquaplanet. *J. Adv. Model. Earth Syst.*, 4,
672 doi:10.1029/2012MS000199.

673 Nordeng, T. 1994. Extended versions of the convective parameterization scheme at
674 ECMWF and their impact on the mean and transient activity of the model in the
675 tropics, in *Tech. Memo.*, 206, Eur. Cent. For Medium-Range Weather Forecasts,
676 Reading, U. K.

677 Peters, K., C. Jakob, L. Davies, B. Khouider, and A. J. Majda (2013), Stochastic behavior
678 of tropical convection in observations and a multicloudmodel, *J. Atmos. Sci.*, 70(11),
679 3556–3575, doi:10.1175/JAS-D-13-031.1

680 Peters, K., C. Crueger, C. Jakob, and B. Mobis. 2017. Improved MJO-simulation in
681 ECHAM6.3 by coupling a stochastic multicloud model to the convection scheme. *J.*
682 *Adv. Model. Earth Syst.*, 9: 193-219.

683 Randall, D., M. Khairoutdinov, A. Arakawa, and W. Grabowski. 2003. Breaking the cloud
684 parameterization deadlock. *Bull. Am. Meteorol. Soc.*, 84: 1547-1564.

685 Rui, H., and B. Wang. 1990. Development characteristics and dynamic structure of
686 tropical intraseasonal convection anomalies. *J. Atmos. Sci.*, 47: 357-379.

687 Satoh M., T. Matsuno, H. Tomita, and coauthors, 2008. Nonhydrostatic ICosahedral
688 Atmospheric Model (NICAM) for global cloud resolving simulations. *J. Comp. Phys.*,
689 227: 3486-3514.

690 Slingo, J. M., K. R. Sperber, J. S. Boyle, J.-P. Ceron, et al. 1996. Intraseasonal

691 oscillations in 15 atmospheric general circulation models: results from an AMIP
692 diagnostic subproject. *Clim. Dyn.*, 12: 325-357.

693 Sperber, K. R. 2004. Madden-Julian variability in NCAR CAM2.0 and CCSM2.0. *Clim.*
694 *Dyn.*, 23: 259-278.

695 Sperber, K. R., J. M. Slingo, P. M. Inness, and K. M. Lau. 1997. On the maintenance and
696 initiation of the intraseasonal oscillation in the NCEP/NCAR reanalysis and the GLA
697 and UKMO AMIP simulations. *Clim. Dyn.*, 13: 769-795.

698 Stevens, B., M. Giorgetta, M. Esch, T. Mauritsen, et al. 2013. Atmospheric component of
699 the MPI-M earth system model: ECHAM6. *J. Adv. Model. Earth Syst.*, 5: 146-172.

700 Subramanian, A. C., and T. Palmer, 2017. Ensemble superparameterization versus
701 stochastic parameterization: A comparison of model uncertainty representation in
702 tropical weather prediction, *J. Adv. Model. Earth Syst.*, 9: 1231– 1250.

703 Thayer-Calder, K., and D. A. Randall. 2009: The role of convective moistening in the
704 Madden-Julian Oscillation. *J. Atmos. Sci.*, 66: 3297-3312.

705 Tiedtke, M. 1989. A comprehensive mass flux scheme for cumulus parameterization in
706 large-scale models. *Mon. Weather Rev.*, 117: 1779-1800.

707 Thual, S., A. J. Majda, and S. N. Stechmann (2014), A stochastic skeleton model for the
708 MJO, *J. Atmos. Sci.*, 71(2), 697–715.

709 Tseng, K.-C., C.-H. Sui, and T. Li. 2015. Moistening processes for the Madden-Julian
710 Oscillations during DYNAMO/CINDY. *J. Clim.*, 28: 3041-3057.

711 Tseng, W.-L., B.-J. Tsuang, N. S. Keenlyside, H.-H. Hsu, and C.-Y. Tu. 2015. Resolving
712 the upper ocean warm layer improves the simulation of the Madden-Julian oscillation.
713 *Clim. Dyn.*, 44: 1487-1503.

714 Tian, B. J., D. E. Waliser, E. Fetzer, B. Lambriksen, Y. Yung, and B. Wang. 2006.
715 Vertical moist thermodynamic structure and spatial-temporal evolution of the Madden-
716 Julian Oscillation in atmospheric infrared sounder observations. *J. Atmos. Sci.*, 63:
717 2462-2485.

718 Waliser, D. E., M. W. Moncrieff, D. Burridge, et al. 2012. The ‘year’ of tropical
719 convection (May 2008-April 2010): Climate variability and weather highlights. *Bull.*
720 *Amer. Meteorol. Soc.*, 93: 1189-1218.

721 Waliser, D. E., K. Sperber, H. Hendon, D. Kim, M. Wheeler, et al. 2009. MJO simulation
722 diagnostics. *J. Clim.*, 22: 3006-3030.

723 Wang, B., and G. Chen. 2017. A general theoretical framework for understanding
724 essential dynamics of Madden-Julian Oscillation. *Clim. Dyn.*, 49: 2309-2328.

725 Wang, B., and S.-S. Lee. 2017. MJO propagation shaped by zonal asymmetric structures:
726 Results from 24-GCM simulations. *J. Clim.*, 30: 7933-7952.

727 Wang, B., S.-S. Lee, D. E. Waliser, C. Zhang, A. Sobel, E. Maloney, T. Li, X. Jiang, and
728 K.-J. Ha. 2018. Dynamics-oriented diagnostics for the Madden-Julian Oscillation. *J.*
729 *Clim.*, 31: 3117-3135.

730 Wang, B., F. Liu, and G. Chen, 2016a. A trio-interaction theory for Madden-Julian
731 Oscillation. *Geosci. Lett.*, 3:34.

732 Wang, S. G., A. H. Sobel, and J. Nie. 2016b. Modeling the MJO in a cloud-resolving
733 model with parameterized large-scale dynamics: Vertical structure, radiation, and
734 horizontal advection of dry air. *J. Adv. Model. Earth Syst.*, 8: 121-139.

735 Wang, B., and X. Xie. 1997. Coupled modes of the warm pool climate system. Part I: The
736 role of air-sea interaction in maintaining Madden-Julian oscillation. *J. Clim.*, 8: 2116-

737 2135.

738 Weikmann K. M, G. R. Lussy, and J. E. Kutzbach, 1985. Intraseasonal (30-60 Day)

739 Fluctuations of Outgoing Longwave Radiation and 250 mb Streamfunction during

740 Northern Winter. *Mon. Wea. Rev.*, 113: 941-961.

741 Wheeler, M. C., and H. H. Hendon, 2004. An all-season real-time multivariate MJO

742 index: Development of an index for monitoring and prediction. *Mon. Wea. Rev.*, 132:

743 1917-1932.

744 Wheeler, M., and G. N. Kiladis. 1999. Convectively coupled equatorial waves: Analysis

745 of clouds and temperature in the wavenumber-frequency domain. *J. Atmos. Sci.*, 56:

746 374-399.

747 Yoneyama, K., C. Zhang, C. N. Long. 2013. Tracking pulses of the Madden-Julian

748 Oscillation. *Bull. Amer. Meteorol. Soc.*, 94: 1871-1891.

749 Zhang, C. 2005. Madden-Julian Oscillation. *Rev. Geophys.*, 43, RG2003.

750 Zhang, C. 2013. Madden-Julian Oscillation: Bridging weather and climate. *Bull. Amer.*

751 *Meteorol., Soc.*, 94: 1849-1870.

752 Zhang, C., and M. Dong. 2004. Seasonality of the Madden-Julian Oscillation. *J. Clim.*,

753 17: 3169-3180.

754

755

756

757

758

759

760 Table and Figure Captions

761 Fig. 1 Difference of annual precipitation (mm/day) of (a) ECHAM_SMCM_ORI and (b)
762 ECHAM_SMCM T31L47 relative to GPCP. (c) Difference between ECHAM_SMCM
763 and ECHAM_SMCM_ORI.

764 Fig. 2 Eastward propagation of MJO precipitation as indicated by the lead-lag correlation
765 of 20-70 day filtered precipitation averaged over 10°S-10°N with reference to the
766 precipitation at the equatorial eastern Indian Ocean (10°S-10°N, 80°E-100°E) during
767 boreal winter (NDJFMA): (a) observation, (b) ECHAM_CTRL, and (c)
768 ECHAM_SMCM. The red contour in (a) represents correlation coefficient (CC) of
769 ± 0.2 .

770 Fig. 3. Propagation of the boundary layer moisture convergence (BLMC) by the lead-lag
771 correlation of 20-70 day filtered BLMC (day^{-1}) averaged over 10°S-10°N with
772 reference to the BLMC at the equatorial eastern Indian Ocean (10°S-10°N, 80°E-
773 100°E) of (a) Observation, (b) ECHAM_CTRL, and (c) ECHAM_SMCM. The red
774 contour in (a) represents correlation coefficient (CC) of ± 0.2 . The brown contours in
775 (a), (b), and (c) represent the lag-longitude correlation map of precipitation.

776 Fig. 4 Zonal asymmetry in the low-level circulation of 850 hPa winds (m/s; vector) and
777 zonal wind speed (m/s; shading) of (a) Observation, (b) ECHAM_CTRL, (c)
778 ECHAM_SMCM; and (d) comparison of the longitudinal variations of the U850 in
779 observation and model results. The structures are the 20-70-day filtered 850-hPa zonal
780 winds and divergence regressed onto the 20-70-day filtered precipitation at the
781 equatorial EIO (10° S-10° N and 80-100° E).

782 Fig. 5 Zonal asymmetry of the vertical structures of equivalent potential temperature

783 anomalies (EPT; K) of (a) Observation, (b) ECHAM_CTRL, (c) ECHAM_SMCM;
784 and (d) Longitudinal variations of the difference of EPT between 850 hPa and 400
785 hPa. The vertical structures are averaged between 5° S and 5° N, which are the 20-70-
786 day filtered EPT fields regressed onto the 20-70-day filtered precipitation in the
787 equatorial EIO (10° S-10° N, 80-100° E).

788 Fig. 6 Zonal asymmetry in diabatic heating (K/day) averaged between 5°S-5°N in (a)
789 observation, (b) ECHAM_CTRL, and (c) ECHAM_SMCM. The vertical structures
790 are the 20-70-day filtered fields regressed onto 20-70-day filtered precipitation in the
791 equatorial EIO (10° S-10° N, 80-100° E).

792 Fig. 7 The 200 hPa winds (m/s; vector), divergence (day⁻¹; contour), and the 300
793 hPa diabatic heating (K/day; shading) in (a) observation, (b) ECHAM_CTRL, and (c)
794 ECHAM_SMCM. The structures are the 20-70-day filtered fields regressed onto the
795 20-70-day filtered precipitation at the equatorial EIO (10° S-10° N and 80-100° E).

796 Fig. 8 Vertical structure of Eddy available potential energy (APE) generation rate
797 (K²/day) averaged between 5°S-5°N in (a) observation, (b) ECHAM_CTRL, and (c)
798 ECHAM_SMCM. The structures are the 20-70-day filtered APE fields regressed onto
799 the 20-70-day filtered precipitation at the equatorial EIO (10° S-10° N and 80-100° E).

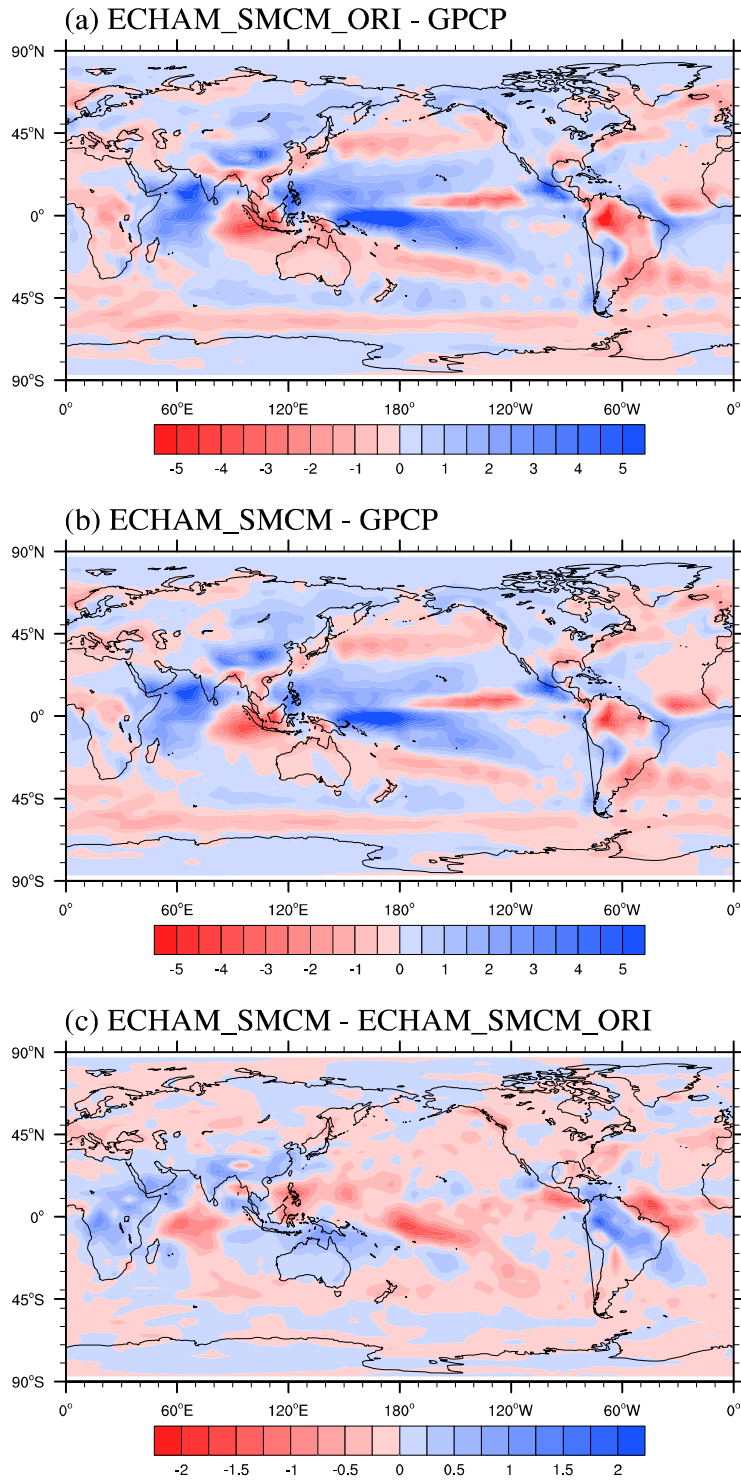
800 Table 1 Pattern correlation coefficient (PCC) and normalized root-mean-square error
801 (NRMSE) between observation and model results.

802

803

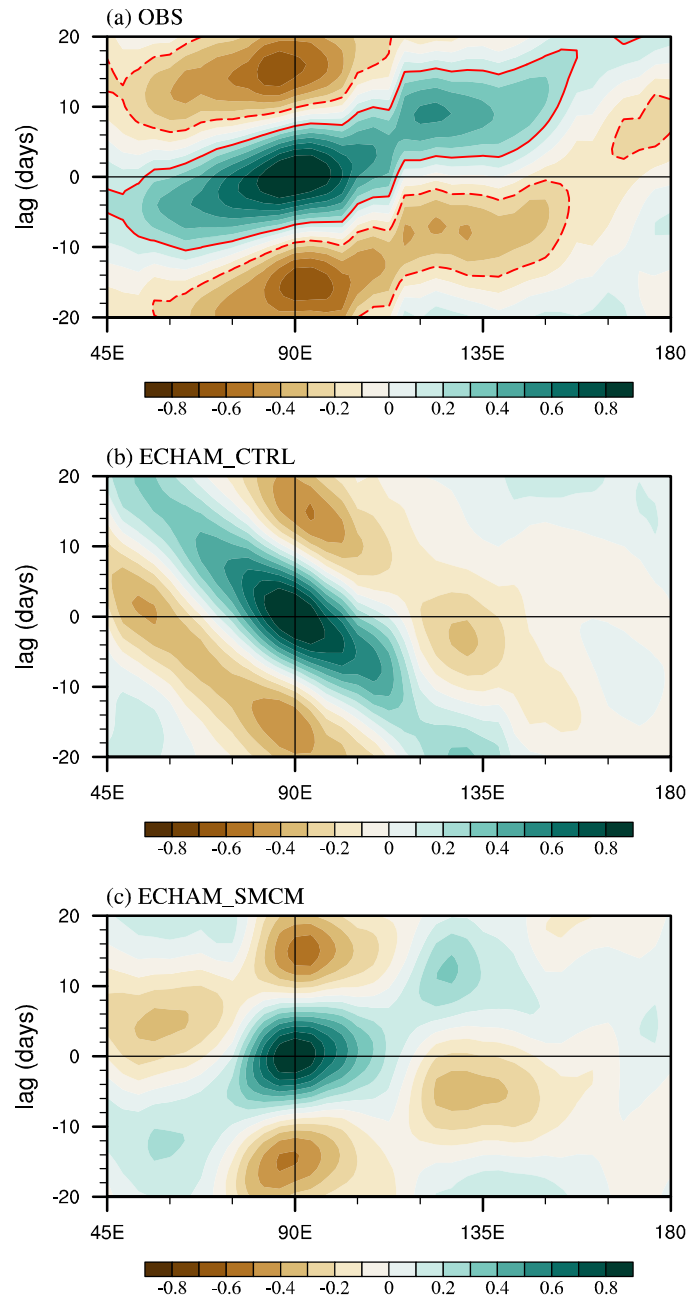
804

805



806

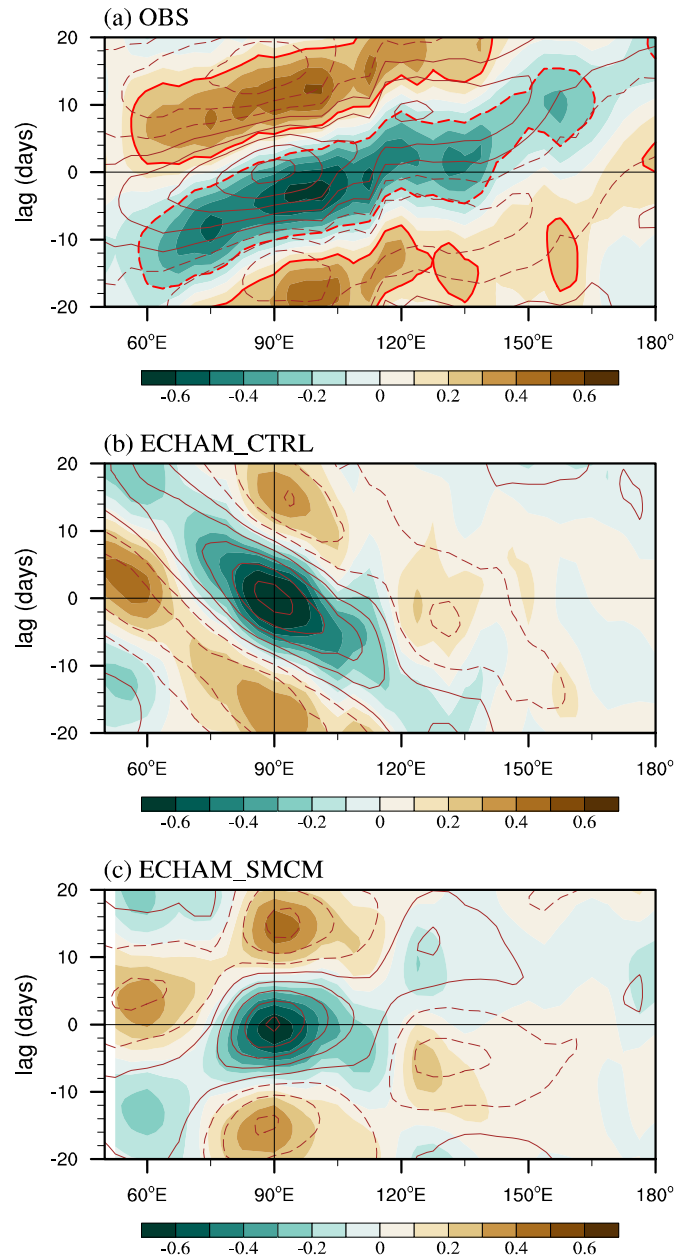
807 Fig. 1 Difference of annual precipitation (mm/day) of (a) ECHAM_SMCM_ORI and (b)
 808 ECHAM_SMCM T31L47 relative to GPCP. (c) Difference between ECHAM_SMCM
 809 and ECHAM_SMCM_ORI.



811

812 Fig. 2 Eastward propagation of MJO precipitation as indicated by the lead-lag correlation
 813 of 20-70 day filtered precipitation averaged over 10°S-10°N with reference to the precipi-
 814 tation at the equatorial eastern Indian Ocean (10°S-10°N, 80°E-100°E) during boreal
 815 winter (NDJFMA): (a) observation, (b) ECHAM_CTRL, and (c) ECHAM_SMCM. The
 816 red contour in (a) represents correlation coefficient (CC) of ± 0.2 .

817



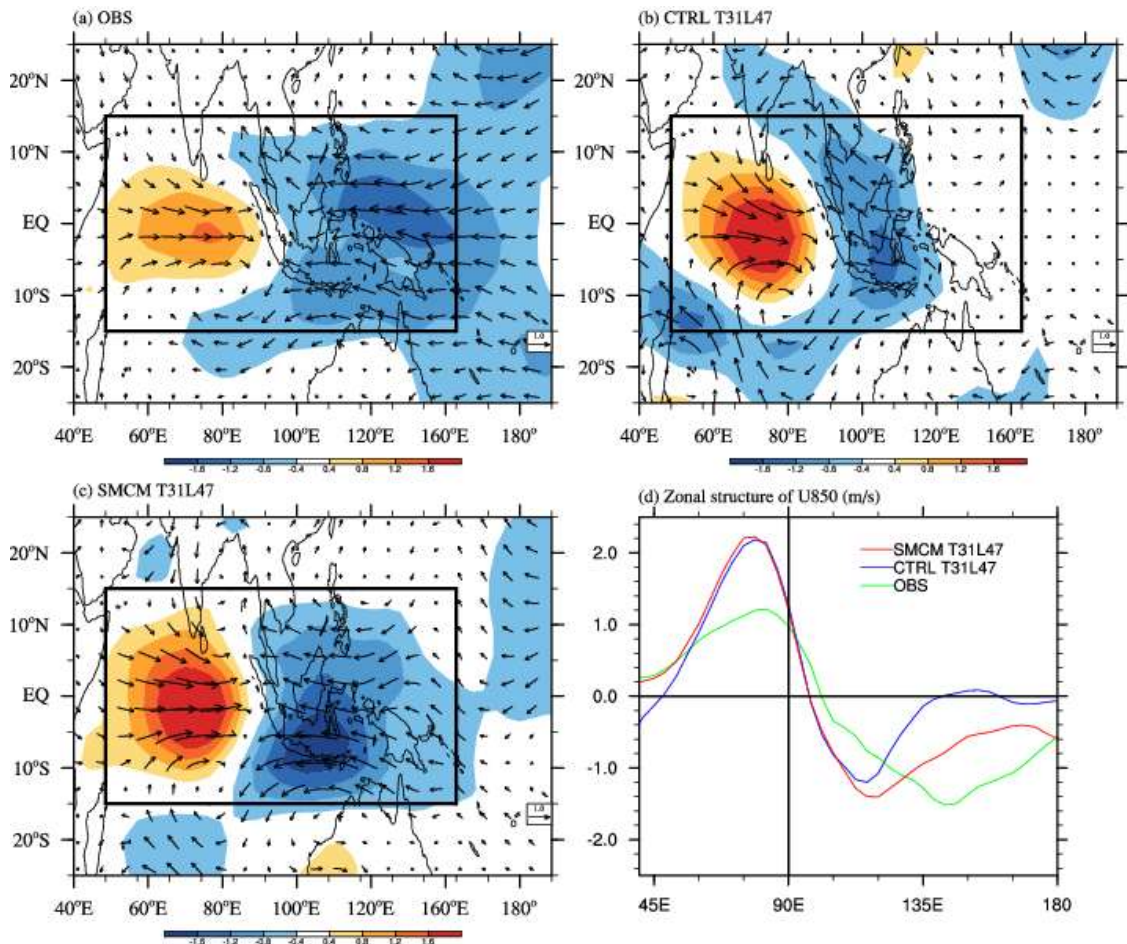
818

819 Fig. 3. Propagation of the boundary layer moisture convergence (BLMC) by the lead-lag
 820 correlation of 20-70 day filtered BLMC (day^{-1}) averaged over 10°S - 10°N with reference
 821 to the BLMC at the equatorial eastern Indian Ocean (10°S - 10°N , 80°E - 100°E) of (a) Ob-
 822 servation, (b) ECHAM_CTRL, and (c) ECHAM_SMCM. The red contour in (a) repre-
 823 sents correlation coefficient (CC) of ± 0.2 . The brown contours in (a), (b), and (c) repre-
 824 sent the lag-longitude correlation map of precipitation.

825

826

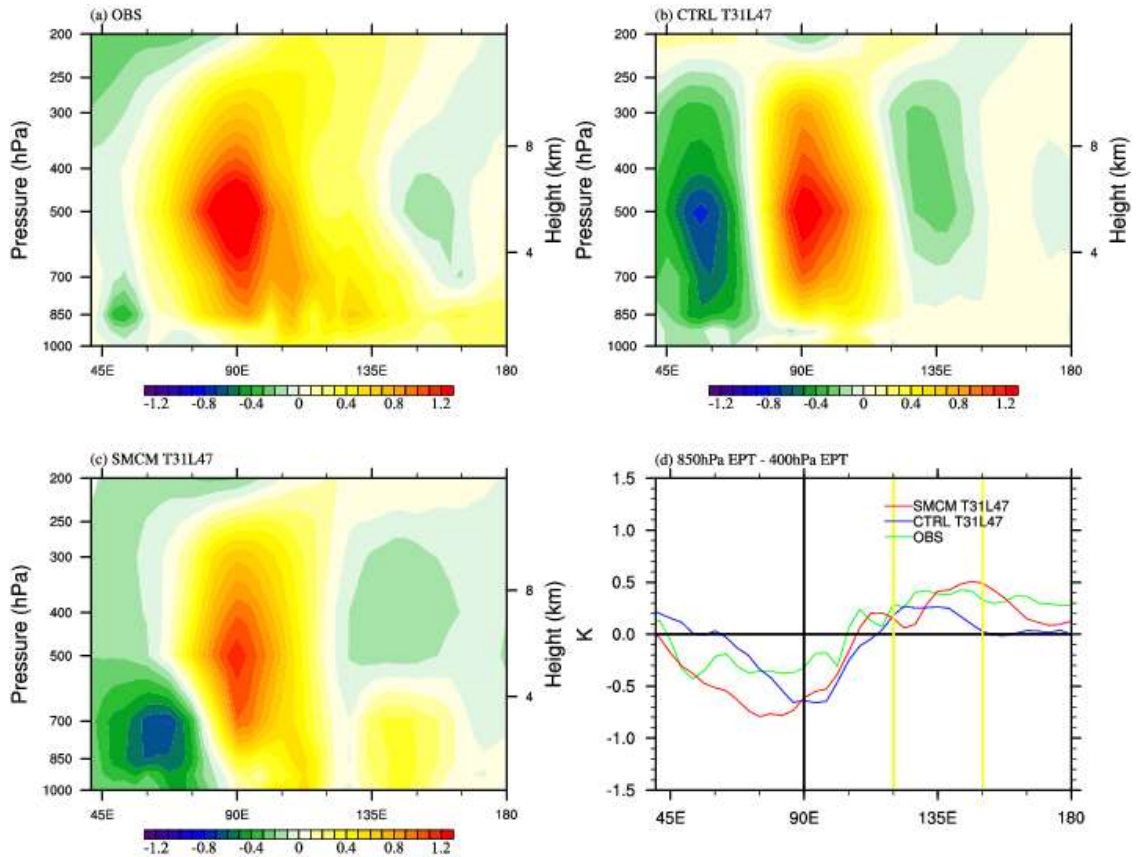
827
828
829
830



831
832 Fig. 4 Zonal asymmetry in the low-level circulation of 850 hPa winds (m/s; vector) and
833 zonal wind speed (m/s; shading) of (a) Observation, (b) ECHAM_CTRL, (c)
834 ECHAM_SMCM; and (d) comparison of the longitudinal variations of the U850 in ob-
835 servation and model results. The structures are the 20-70-day filtered 850-hPa zonal
836 winds and divergence regressed onto the 20-70-day filtered precipitation at the equatorial
837 EIO (10° S-10° N and 80-100° E).

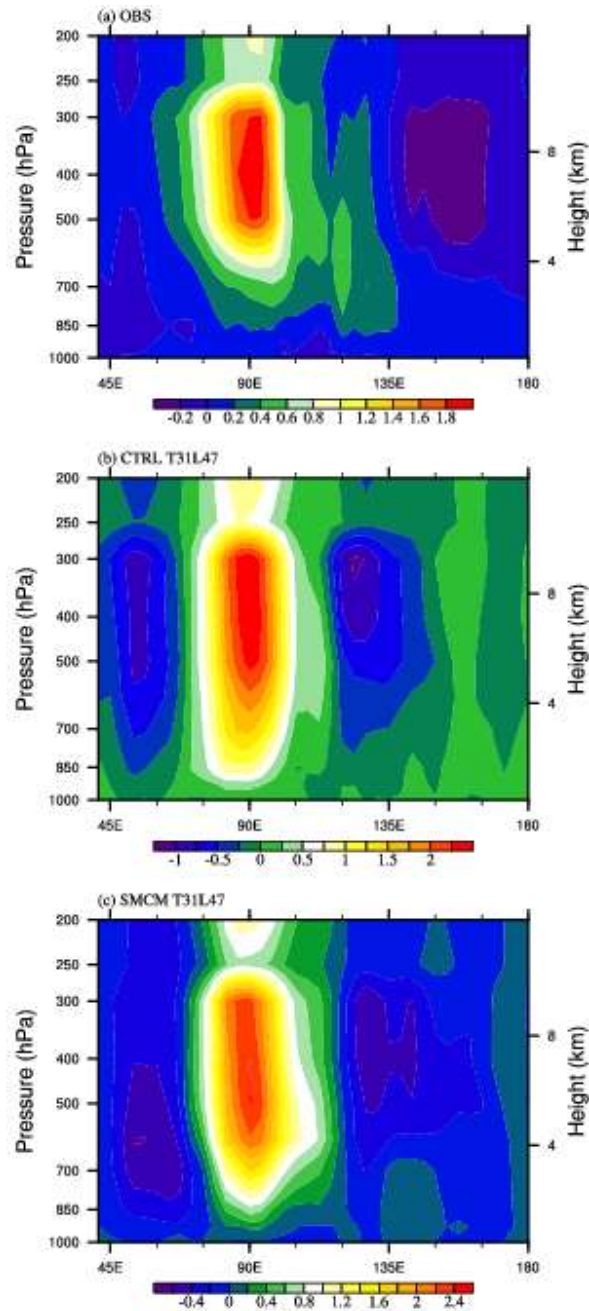
838
839
840

841
842
843
844



845
846 Fig. 5 Zonal asymmetry of the vertical structures of equivalent potential temperature
847 anomalies (EPT; K) of (a) Observation, (b) ECHAM_CTRL, (c) ECHAM_SMCM; and
848 (d) Longitudinal variations of the difference of EPT between 850 hPa and 400 hPa. The
849 vertical structures are averaged between 5° S and 5° N, which are the 20-70-day filtered
850 EPT fields regressed onto the 20-70-day filtered precipitation in the equatorial EIO (10°
851 S-10° N, 80-100° E).

852
853
854
855
856



857

858 Fig. 6 Zonal asymmetry in diabatic heating (K/day) averaged between 5°S-5°N in (a) ob-
 859 servation, (b) ECHAM_CTRL, and (c) ECHAM_SCM. The vertical structures are the
 860 20-70-day filtered fields regressed onto 20-70-day filtered precipitation in the equatorial
 861 EIO (10° S-10° N, 80-100° E).

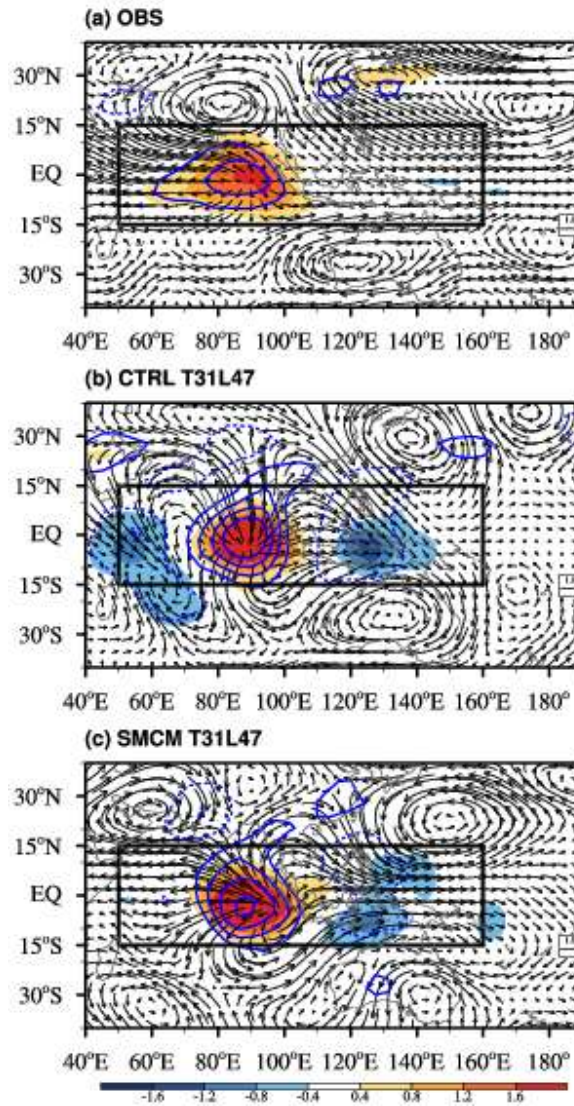
862

863

864

865

866



867

868 Fig. 7 The 200 hPa winds (m/s; vector), divergence (day^{-1} ; contour), and the 300 hPa dia-

869 batic heating (K/day; shading) in (a) observation, (b) ECHAM_CTRL, and (c)

870 ECHAM_SMCM. The structures are the 20-70-day filtered fields regressed onto the 20-

871 70-day filtered precipitation at the equatorial EIO (10°S - 10°N and 80°E - 100°E).

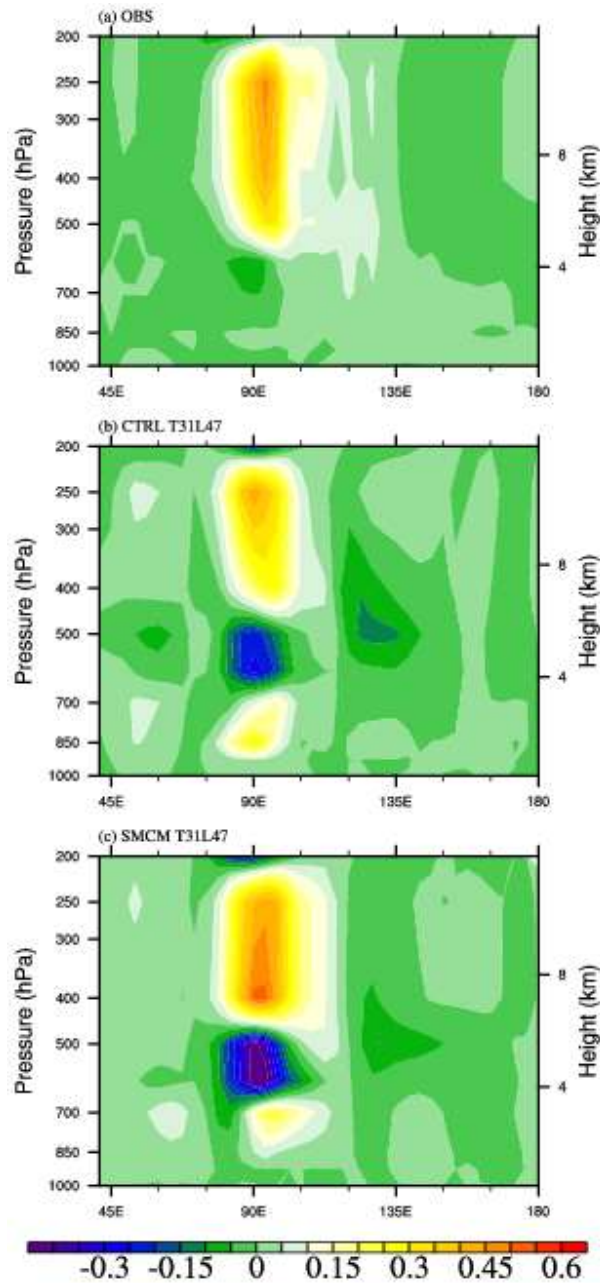
872

873

874

875

876



877

878 Fig. 8 Vertical structure of Eddy available potential energy (APE) generation rate
879 (K^2/day) averaged between $5^{\circ}S-5^{\circ}N$ in (a) observation, (b) ECHAM_CTRL, and (c)
880 ECHAM_SMCM. The structures are the 20-70-day filtered APE fields regressed onto the
881 20-70-day filtered precipitation at the equatorial EIO ($10^{\circ}S-10^{\circ}N$ and $80-100^{\circ}E$).

882

883 Table 1 Pattern correlation coefficient (PCC) and normalized root-mean-square error
 884 (NRMSE) between observation and model results.

| Diagnostic fields | T31L47 | | T63L47 | |
|--|---------------------------|---------------------------|---------------------------|---------------------------|
| | EHCAM CTRL PCC (NRMSE) | ECHAM SMCM PCC (NRMSE) | ECHAM CTRL PCC (NRMSE) | ECHAM SMCM PCC (NRMSE) |
| Propagation of precipitation (EIO) | 0.14 (1.02) | 0.76 (0.62) | 0.15 (1.00) | 0.70 (0.71) |
| Propagation of precipitation (WPO) | 0.68 (0.67) | 0.82 (0.54) | 0.66 (0.69) | 0.79 (0.58) |
| Propagation of BLMC (EIO) | 0.11 (1.06) | 0.73 (0.70) | 0.15 (1.02) | 0.78 (0.73) |
| Propagation of BLMC (WP) | 0.62 (0.75) | 0.80 (0.58) | 0.73 (0.65) | 0.82 (0.53) |
| Horizontal structure of U850 | 0.66 (1.01) | 0.87 (0.76) | 0.69 (0.88) | 0.81 (0.66) |
| Vertical structure of EPT | 0.66 (1.01) | 0.87 (0.76) | 0.70 (1.10) | 0.75 (0.86) |
| Vertical structure of diabatic heating | 0.61 (1.20) | 0.82 (0.85) | 0.67 (1.06) | 0.71 (0.86) |
| Horizontal structure of 200 hPa divergence | 0.68 (1.53) | 0.78 (1.09) | 0.75 (1.30) | 0.80 (1.00) |
| Horizontal structure of 300 hPa diabatic heating | 0.78 (0.98) | 0.87 (0.80) | 0.80 (0.90) | 0.84 (0.75) |
| Vertical structure of eddy APE generation | 0.40 (1.11) | 0.55 (1.17) | 0.59 (0.87) | 0.68 (0.76) |

885

886

887